

Design-Based Assessment of Continuous Coaxial DED Nozzles Considering Substrate-Induced Gas Flow Effects

Mehmet Ermurat ✉ – Muhammet Ibrahim Asci – Ibrahim Hakki Ince
Kahramanmaras Sutcu Imam University, Türkiye
✉ ermurat@ksu.edu.tr

Abstract *Continuous coaxial nozzles are widely used in directed energy deposition (DED) processes. However, many numerical studies rely on substrate-free free-jet models that fail to capture critical gas–surface interactions. This study presents a design-oriented investigation of continuous coaxial DED nozzles by examining the influence of nozzle geometry and gas flow interactions under realistic deposition conditions. A three-dimensional CFD framework incorporating particle tracing was applied, in which a physical substrate was explicitly included at the intended standoff distance to account for stagnation pressure formation, gas rebound, and near-wall flow effects. Two nozzle geometries, a narrow nozzle (β = 24°) and a wide nozzle (β = 35°), were evaluated under varying carrier and shaping gas velocities relative to a fixed optical shielding gas velocity. Powder convergence behavior was quantified using a layered particle counting strategy and analyzed through number density distributions in the focal region. The results show that nozzle geometry strongly governs powder focusing behavior. The narrow nozzle consistently produced a compact and axisymmetric powder stream with higher catchment efficiency, whereas the wide nozzle exhibited diffuse flow patterns and reduced focal coherence. Excessive shaping gas velocities were found to degrade convergence by expanding the substrate-induced stagnation pressure zone. These findings provide a physics-based rationale for geometry-dependent nozzle selection in continuous coaxial DED applications.*

Keywords *directed energy deposition (DED); additive manufacturing; particle tracing; continuous coaxial nozzle design*

Highlights

- *Substrate-induced gas–surface interactions are explicitly modeled in coaxial DED nozzles.*
- *Narrow-angle nozzles offer significantly higher powder efficiency than wide-angle designs.*
- *Excessive shaping gas velocity expands stagnation pressure and degrades powder focusing.*
- *Geometry-dependent gas flow optimization governs powder catchment and focal stability.*

1 INTRODUCTION

Directed energy deposition (DED) processes, whether utilizing wire or powder feedstocks, facilitate the layer-by-layer fabrication of metallic components by delivering material directly into a localized energy source to generate a stable melt pool on a substrate. Within the specific context of powder-fed laser DED systems, consistent powder transport through the nozzle, culminating in precise injection into the laser–material interaction zone, is essential for effective consolidation. The fundamental nature of this process is heavily dictated by the dynamics of powder delivery, specifically regarding flow stability, carrier gas behavior, and spatial particle distribution. Consequently, these factors serve as primary determinants for the resulting build quality, dimensional tolerances, and overall melt pool stability. Because the nozzle architecture dictates the fluid dynamics of both the shielding gas and the powder stream, it stands as a critical subsystem influencing process efficiency and material utilization. Despite these advancements, achieving a truly homogeneous and stable powder delivery remains a formidable challenge, primarily complicated by flow fluctuations, particle agglomeration, and the inherent sensitivity to varying powder morphologies [1-7]. Figure 1 illustrates the powder-fed laser additive manufacturing method [5].

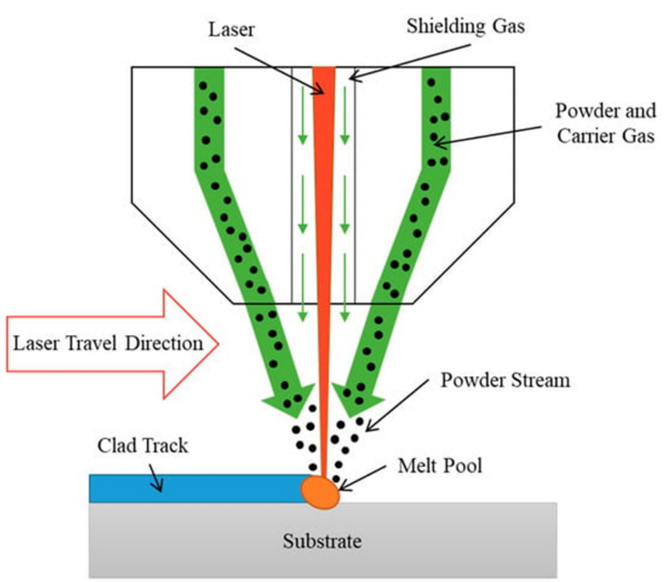

Fig. 1. DED diagram [5]

Powder feeding nozzles are categorized based on the orientation of the powder material and the energy source during feeding into the processing zone [8-11]. Different nozzle designs are shown in Fig. 2 [12-14]. An example of a nozzle design where the energy source is focused from the periphery and the powder material is fed from the center of the nozzle as called annular laser beam nozzle is schematically shown in Fig. 2a. Examples of nozzle types where the energy source is focused from the center include the lateral feed nozzle, schematically shown in Fig. 2b, the discrete coaxial nozzle in Fig. 2c, and the continuous coaxial nozzle in Fig. 2d.

Continuous coaxial nozzles feature a single annular exit that generates a continuous cone-shaped powder flow and have been widely investigated in recent academic studies [10,15-22]. In these

 DOI: 10.5545/sv-jme.2026.1646

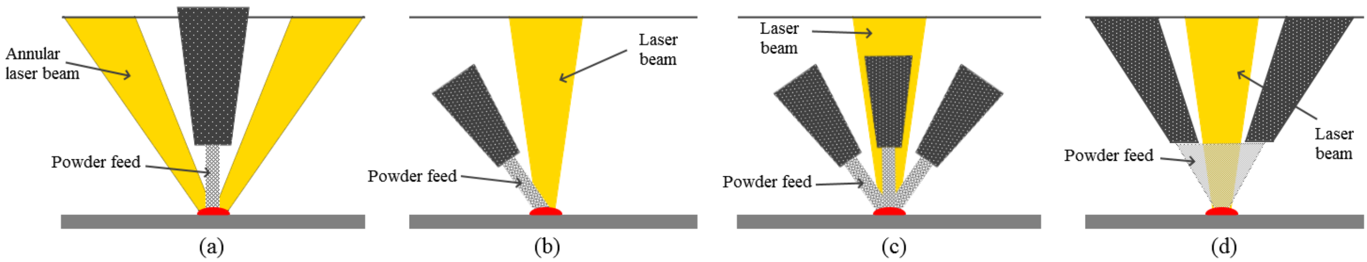

Fig. 2. Some DED nozzle types: a) annular laser beam nozzle, b) lateral nozzle, c) discrete coaxial nozzle, and d) continuous coaxial nozzle; adapted from [12-14]

nozzles, the powder flow converges coaxially with the laser beam at the focal region. Powder is delivered to this region via a carrier gas through a circular channel, surrounding the laser beam and thereby promoting uniform powder distribution [9]. Simultaneously, a shaping gas is integrated into the system through a second circular channel to enhance the concentration of powders toward the focal region [11].

The symmetrical powder flow from a circular structure toward the laser offers significant advantages in powder-fed DED processes compared to other nozzle types, primarily due to its direction-independent powder feeding capability, homogeneous particle distribution, and high catchment efficiency [23,24]. However, it also has challenges, such as the required high geometric precision of the internal channel structure, the necessity of ensuring a careful control of the gas-to-powder ratio, and manufacturing complexity [11].

In powder-fed DED, powder flow is controlled by nozzle design and the flow rates and resulting flow velocities of carrier, optical shielding, and shaping/protection gases, with coaxial nozzles generating a characteristic powder flow structure that evolves as particles exit the nozzle and interact with the surrounding gas streams [15]. As depicted in Fig. 3, powder particles emerge from the nozzle in a distinct annular distribution, subsequently gravitating toward the central axis as a result of the complex interplay between nozzle geometry and gas-phase dynamics. The region immediately succeeding the nozzle exit, characterized by the inward trajectory of particles, is defined as the diffusion (or annular) zone. As the flow progresses downstream, these powder streams intersect at the central axis, establishing the convergence zone—a region defined by peak particle density. Beyond this focal point, the momentum and inertia of the particles cause a radial scattering effect, resulting in the divergence (or dispersed) zone, in which the powder stream gradually spreads outward from the central axis [23,25,26].

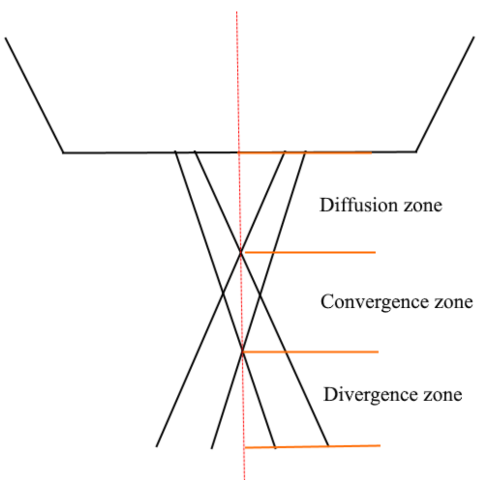

Fig. 3. Powder flow zones; adapted from [23,26]

The convergence zone, also referred to in the literature as the concentration or consolidation zone, defines the optimal location for substrate placement in DED, as it directly governs powder catchment and deposition efficiency. The exact spatial position and confinement of this zone relative to both the nozzle tip and the melt pool are heavily dependent on nozzle design, gas flow angles, and the resultant velocities of the process gases. Consequently, generating a uniformly narrow convergence zone, ideally matching the dimensions of the laser spot, stands as a fundamental requirement for maximizing deposition performance and powder delivery [11,22,27-29]. However, in practice, localized turbulence arising from intricate gas–particle interactions near the melt pool tends to distort particle flight paths. This aerodynamic interference invariably causes premature scattering, which in turn degrades material utilization rates [18,26,30]. This effect becomes more severe when the convergence distance is large or when gas flow rates are insufficient to maintain particle momentum [31].

The convergence distance is defined as the axial distance from the nozzle exit to the geometric focal point of the converging powder streams and is primarily governed by nozzle geometry, particularly the annular angle. In contrast, the effective convergence distance, the true spatial zone where particle coalescence takes place, is inherently dynamic and closely coupled with the intricate interplay between the powder feed rate and gas flow parameters, namely the carrier, shielding, and shaping gas flow rates. To ensure steady powder delivery alongside optimal catchment efficiency, managing this effective convergence distance is critical; it must be carefully constrained to prevent it from surpassing the physical standoff distance established between the nozzle tip and the substrate.

The intricate interdependence between nozzle geometry and gas flow parameters heavily dictates the spatial distribution of particles and the subsequent density within the convergence zone. Among these operational variables, the carrier gas flow rate acts as a dominant driver causing the actual convergence point to deviate from its theoretical geometric position. Increasing the carrier gas flow rate, typically to values in the range of 6 L/min to 8 L/min, enhances particle momentum and velocity, thereby promoting particle coalescence and the formation of a well-defined convergence zone. However, excessively high carrier gas flow rates (e.g., >8 L/min) inevitably induce fluid turbulence within the gas–powder stream, which triggers pronounced particle spreading and a corresponding drop in convergence zone density [31]. On the other hand, an insufficient carrier gas flow rate (e.g., 2 L/min) fails to impart the requisite momentum to the feedstock, yielding a diffuse, poorly defined powder stream. The exact nature of this degradation is closely tied to the specific nozzle diameter, the resulting orifice area, and the powder size distribution. Ultimately, these insights underscore the necessity of a coupled optimization methodology to strike a balance between fixed nozzle architectures and fluid-dynamic process parameters.

Elevating the carrier gas flow rate shifts the optimal convergence distance further downstream, a phenomenon directly driven by enhanced particle momentum and subsequent jet spreading. This behavior underscores the necessity for a synergistic optimization of nozzle architecture and fluid-dynamic parameters, ensuring effective powder concentration precisely at the substrate center. Earlier investigations consistently demonstrate that achieving high-efficiency powder delivery relies on confining the powder stream within the boundaries of the laser beam diameter at the convergence zone; such spatial confinement is essential for maximizing powder catchment and driving up overall deposition efficiency.

Beyond flow convergence, melt pool dynamics introduce an additional loss mechanism via sputter generation, thereby further affecting powder delivery efficiency. When carrier gas flow rates are elevated, the resulting intensification of particle momentum can potentially exacerbate this sputter formation, ultimately detrimental to effective powder utilization. So, powder flow convergence and sputter suppression should be jointly optimized.

Parallel to carrier gas effects, the shielding gas discharges outward from the nozzle center, primarily aimed at isolating the melt pool and protecting the laser optics, yet its flow has been documented to interfere with powder convergence by destabilizing the central particle concentration. As shielding gas flow rates escalate, this aerodynamic interference intensifies, driving pronounced particle dispersion away from the intended focal region and inadvertently compromising convergence efficiency. Conversely, the shaping gas acts as a confining force, directed inward toward the powder stream to narrow its trajectory and boost focusing efficiency. This corrective effect, however, operates within a delicate window; excessively high shaping gas flow rates risk triggering localized fluid turbulence within the gas–powder stream, which ultimately induces lateral particle scattering and degrades the overall convergence quality.

Designing effective nozzles for DED applications remains an intricate task, largely because the underlying physics demands managing highly dynamic powder transport within a turbulent gas medium, coupled with complex flow channel profiles and erratic post-exit particle trajectories [26]. As a result, isolating nozzle geometry from fluid parameters is unfeasible; architectural features, most notably the annular angle and geometric convergence distance, must be integrated into a holistic design framework that simultaneously accounts for carrier, shielding, and shaping gas flow rates to secure robust powder focusing and predictable deposition performance.

In light of these intricate and highly coupled physical phenomena, computational fluid dynamics (CFD) has emerged as an essential methodology for deconstructing and optimizing powder flow behavior [32]. Given that evaluating a multitude of interacting operational variables through purely empirical testing is both cost-prohibitive and time-intensive, numerical simulations offer a viable alternative; they yield granular insights into gas-phase dynamics and discrete powder transport phenomena, particularly regarding localized particle velocities and spatial concentration distributions [25,30,31]. Furthermore, these models enable the prediction of particle–laser interactions and laser energy attenuation, supporting the optimized design of nozzle configurations prior to experimental implementation [30,33].

Notwithstanding these computational strides, a profound gap persists within the existing literature. A vast majority of numerical investigations [10,11,18,19,23,28,30,33,34] rely on simplified free-domain assumptions, treating the gas–powder stream effectively as an unconstrained ‚free jet‘ [25,35-37] that propagates without encountering a physical substrate. Such boundaries, however, are omnipresent in actual DED operations, where material is continuously deposited onto either a base substrate or prior layers. Neglecting the substrate prevents accurate representation of the pressure distribution, velocity gradients, aerodynamic interactions, and turbulent backflows generated near the deposition region. As highlighted by [15], this simplification limits the predictive capability of existing models under realistic deposition conditions.

While rare studies such as [38] have addressed substrate interaction, revealing that the substrate increases powder concentration through a rebound mechanism, they remain limited in scope regarding the aerodynamic sweeping effect caused by the positive stagnation pressure formed on the surface. This localized pressure field inherently tends to deflect lighter particles away from the central axis, a behavior whose exact correlation with the structural parameters of the nozzle remains largely uncharted. Similarly, although the work of [39] validated that intense particle ricochet substantially disrupts focusing stability, their scope was restricted to discrete nozzle configurations. This leaves a significant knowledge deficit regarding continuous coaxial systems, which by nature introduce far more complex aerodynamic barriers and cross-flow interactions near the deposition zone.

In this context, this study addresses the identified methodological gap through the development and evaluation of an optimized continuous coaxial nozzle design tailored to the operational constraints of the employed laser system. Unlike conventional approaches, a substrate is explicitly incorporated at the prescribed standoff distance as an active boundary condition within a CFD framework based on Lagrangian particle tracing. In addition, unlike many previous studies employing two dimensional (2D) axisymmetric models, the present work utilizes a full 3D model to more accurately capture the mixing behavior of gases entering from different inlet locations and feed rates within the annular nozzle channel, as well as their subsequent interaction with the surrounding atmosphere after exiting the nozzle. The study systematically investigates the effects of annular powder channel angle and gas flow parameters (carrier and shaping gas) as primary design variables. By explicitly accounting for particle rebound and stagnation-induced aerodynamic interactions near the substrate, the proposed approach enables more precise control of the powder consolidation zone and improves powder catchment efficiency, ultimately enhancing deposition quality in DED processes.

2 METHODS AND MATERIALS

2.1 Nozzle Design and Geometrical Configurations

The DED system employed in this study consists of a commercial manual laser welding torch integrated with a custom-designed continuous coaxial nozzle. As shown in Fig. 4, the design features three functional channels: a central optical shielding gas channel, an annular powder-gas flow channel, and a peripheral shaping gas channel. Both the annular and peripheral channels are equipped with four symmetrically positioned inlets to ensure flow uniformity. The central cavity enables the laser beam to reach the process zone while protecting the optics [16].

The nozzle's performance is primarily governed by the annular angle (β) of the powder feeding channel. This angle determines the theoretical convergence of the powder stream at a constant stand-off distance of 10.85 mm. For this study, two distinct nozzle designs were developed with conical angles (β) of 24° (narrow) and 35° (wide), as illustrated in Fig. 4.

Ti6Al4V alloy powder with a particle size range of 77 µm to 109 µm (average diameter 90 µm) was used with high-purity Argon as the carrier, shielding, and shaping gas. The powder feed rate was kept constant at 11 g/min to ensure consistency.

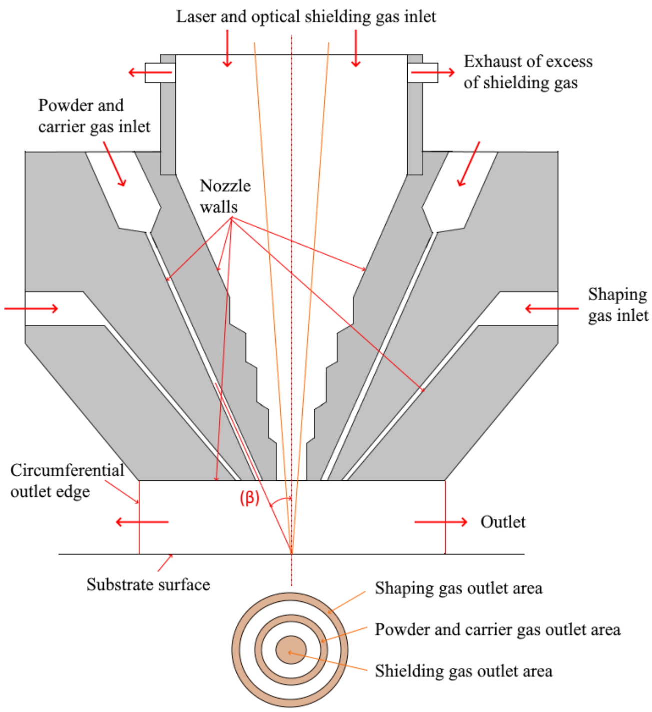

Fig. 4. Designed nozzle and parameters

A velocity-based approach was adopted to ensure precise control over powder behavior across different nozzle geometries, since identical flow rates result in varying velocities depending on the orifice cross-sectional areas. The optical shielding gas flow rate was set at 15 L/min for optical protection. However, to mitigate aerodynamic disturbances, the system was optimized using integrated exhaust outlets at the upper section of the nozzle to provide a net flow of 4 L/min (or a velocity of 6 m/s) at the nozzle tip. The necessity for this configuration was confirmed through preliminary flow analyses, which indicated that excessive shielding gas flow causes powder stream divergence as the high-velocity region overcomes particle momentum. Conversely, insufficient flow allows carrier and shaping gases to enter the optical aperture, resulting in an undesirable upward flow. Consequently, the exhaust plan was optimized to ensure a stable flow at the nozzle tip while preventing these adverse effects.

Furthermore, the study evaluates carrier and shaping gas parameters at velocities of 4 m/s, 6 m/s (baseline), and 8 m/s. This approach aims to analyze how velocity differentials and resulting pressure distributions influence the powder trajectory.

Table 1 summarizes the calculated inlet gas flow rates required to reach these targeted velocities (u) based on the specific orifice areas (A) shown in Fig. 4, as derived from Eq. (1).

$$Q = uA. \quad (1)$$

2.2 Simulation Methodology and Boundary Conditions

The CFD analyses and particle trajectories were simulated using the Particle tracing module of COMSOL Multiphysics. In this study, a coupled approach was employed where the gas flow was solved as a stationary flow field as is does not change overtime, while the particles were simulated using a time-dependent particle tracing solver. The particles are driven by the drag force that has been calculated from the flow field through discrete time steps to account for their time-dependent trajectories. For the bidirectionally coupled (two-way) simulations, the momentum exchange between the gas and particles was calculated by iteratively updating the stationary gas flow with the source terms derived from these time-dependent particle trajectories until statistical convergence was achieved.

Table 1. Calculated inlet flow rates for targeted gas velocities

Nozzle type	Setup no.	Carrier gas inlet flow rate [L/min]	Shaping gas inlet flow rate [L/min]	Nozzle exit gas velocities relative to flow rate and orifice area [m/s]	
				Carrier gas	Shaping gas
Narrow nozzle (β = 24°)	NN1	6.5	7.25	4	4
	NN2	6.5	9.5	4	6
	NN3	6.5	12.5	4	8
	NN4	9.5	7.25	6	4
	NN5	9.5	9.5	6	6
	NN6	9.5	12.5	6	8
	NN7	12.5	7.25	8	4
	NN8	12.5	9.5	8	6
	NN9	12.5	12.5	8	8
Wide nozzle (β = 35°)	WN1	12.25	12.25	4	4
	WN2	12.25	18.5	4	6
	WN3	12.25	24.5	4	8
	WN4	16.5	12.25	6	4
	WN5	16.5	18.5	6	6
	WN6	16.5	24.5	6	8
	WN7	22	12.25	8	4
	WN8	22	18.5	8	6
	WN9	22	24.5	8	8

A computational domain was defined between the nozzle exit and the substrate surface, as shown in Fig. 4. The domain width was selected based on preliminary analyses to match the outer boundary of the manufactured nozzle's lower surface and was kept of identical diameter for both nozzle geometries and the computational domain. This includes the entire powder convergence zone and ensures consistent comparison between designs.

A substrate boundary was placed 10.85 mm below the nozzle exit to represent realistic process conditions and to capture the interaction between the impinging jet and the substrate. This setup allows the development of the flow regime within the actual processing gap and enables evaluation of powder convergence on the deposition region. Ambient pressure outlet conditions were applied to the peripheral boundaries to facilitate gas evacuation. To justify the inclusion of substrate and isolate its impact on fluid dynamics, comparative preliminary baseline gas flow simulations were also conducted for both substrate-free and substrate-induced configurations under identical boundary conditions.

Unlike some previously reported approaches employing either highly confined or expanded open-atmosphere domains [40,41], the computational domain in this study was defined as the region bounded between the nozzle geometry and the substrate to preserve realistic flow development conditions. Preliminary analyses indicated that domains restricted only to the nozzle exit could not fully represent the atmospheric interaction of the emerging flow, whereas excessively large domains introduced unrealistic flow expansion behavior. Therefore, the selected domain size was chosen to preserve the natural flow development between the nozzle and substrate while maintaining computational stability. As illustrated in Fig. 4, ambient pressure was applied as an outlet boundary condition at the peripheral boundaries to facilitate gas evacuation, whereas all remaining surfaces were treated as walls. This configuration allows inward or outward flow depending on the local pressure distribution within the domain.

Literature studies on coaxial DED nozzles generally report turbulent flow behavior under typical processing conditions [15,22,25,30,32,40]. As part of the coupled solver, stationary CFD simulations were performed to evaluate the internal gas flow characteristics of the nozzle. The Reynolds number was calculated based on the hydraulic diameter using Eq. (2).

$$Re = \frac{\rho u D_H}{\mu}, \tag{2}$$

where ρ is the fluid density, u is the mean velocity, D_H is the hydraulic diameter, μ is the dynamic viscosity. The calculated Reynolds number Re was 2.17×10^6, indicating a fully turbulent flow regime.

The interaction between gas flow and particle motion was modeled using the Euler–Lagrange approach. The fluid phase was treated as a continuous medium, whereas the particle phase was tracked discretely. To accurately capture the physics in the high-concentration zones, a bidirectional (two-way) coupling method was implemented. Particle motion was described according to Newton's second law using Eq. (3).

$$\frac{d}{d_t}\left(m_p v\right) = F_D + F_g + F_{ext}, \tag{3}$$

where, m_p is the particle mass, v is the particle velocity, F_D is the drag force, F_g is the gravitational force, F_{ext} represents other external forces. The primary drag force acting on the particles was calculated using Eq. (4).

$$F_D = \frac{1}{2} C_D \rho A_p \left|u - v\right|\left(u - v\right), \tag{4}$$

where C_D is the drag coefficient, A_p is the particle cross-sectional area, and u and v are the fluid and particle velocities, respectively. To accurately determine the drag coefficient (C_D) for the spherical Ti6Al4V particles under the dynamic flow conditions, the empirical Schiller–Naumann drag model was specified within the software framework. This model is highly suitable for the flow regime investigated, where the particle Reynolds number (Re_p) remains well below 800. In this formulation, C_D is calculated using Eq. (5).

$$C_D = \frac{24}{Re_p}\left(1 + 0.15 Re_p^{0.687}\right) \quad for \quad Re_p \le 800, \tag{5}$$

where the particle Reynolds number Re_p, which defines the relative ratio of inertial forces to viscous forces acting on the discrete phase, is expressed as in Eq. (6).

$$Re_p = \frac{\rho \left|u - v\right| d_p}{\mu}, \tag{6}$$

where, d_p represents the mean particle diameter (90 µm), and μ is the dynamic viscosity of the continuous Argon phase.

The continuous fluid phase is governed by the conservation equations of mass and momentum for an incompressible steady flow within a Reynolds-averaged Navier–Stokes (RANS) framework, expressed respectively as follows:

$$\rho \nabla u = 0, \tag{7}$$

$$\rho\left(u\nabla\right)u = \nabla\left[-pI + K\right] + F_v, \tag{8}$$

where u represents the fluid velocity vector, p is the static pressure, I is the identity tensor, and F_v represents the volume forces acting on the fluid, which inherently includes the bidirectional momentum source terms introduced by the discrete particle phase interactions. The viscous stress tensor, denoted as K, and the transport equation for the baseline turbulent kinetic energy k are incorporated into the continuous phase formulation using Eqs. (9) and (10), respectively:

$$K = (\mu + \mu_T)(\nabla_u + (\nabla_u)^T), \tag{9}$$

$$\rho\left(u\nabla\right)k = \nabla\left[\left(\mu + \frac{\mu_T}{\sigma_k}\right)\nabla k\right] + P_k - \rho\varepsilon. \tag{10}$$

The baseline formulations presented above account for the continuous phase dynamics, where μ_T is the turbulent dynamic viscosity. The framework implicitly accounts for the static pressure fields and external body forces, including the bidirectional momentum source terms introduced by the discrete phase interaction. Furthermore, ε is the turbulence dissipation rate, P_k is the volumetric production term of k due to mean velocity gradients, and σ_k is the turbulent Prandtl number for kinetic energy.

To resolve the complex near-wall gradients and anisotropic turbulence inside the narrow channels of the coaxial nozzle, the v^2-f turbulence model was implemented. This model extends the standard $k-\varepsilon$ formulation by introducing transport equations for turbulence dissipation rate (ε), velocity variance (ζ), and the elliptic blending function (α) as expressed in Eqs. (11-13), respectively.

$$\rho\left(u\nabla\right)\varepsilon = \nabla\left[\left(\mu + \frac{\mu_T}{\sigma_\varepsilon}\right)\nabla\varepsilon\right] + \frac{1}{\tau}(C_{\varepsilon 1}\left(\zeta,\alpha\right)P_k - C_{\varepsilon 2}(k,\varepsilon,\alpha)\rho\varepsilon), \tag{11}$$

$$\rho\left(u\nabla\right)\zeta = \nabla\left[\left(\mu + \frac{\mu_T}{\sigma_\zeta}\right)\nabla\zeta\right] + \frac{2}{k}\left(\alpha^3\mu + \frac{\mu_T}{\sigma_k}\right)\nabla k \nabla\zeta + \left(1 - \alpha^3\right)f_w + \alpha^3 f_h - \frac{\zeta}{k}P_k, \tag{12}$$

$$\alpha - L^2\nabla^2\alpha = 1. \tag{13}$$

In these equations, L represents the turbulence length scale. The velocity variance equation Eq. (12) accounts for turbulence fluctuations perpendicular to the walls, while the blending function Eq. (13) transitions the model between near-wall anisotropic restriction and far-field isotropic turbulence behavior.

To simulate the powder transport, 50,000 discrete particles, modelling a constant mass flow rate of 11 g/min, were released into the domain and tracked until all particles settled on the substrate surface or at the outlet boundaries to ensure convergence and accuracy of the results. Although the standard $k-\varepsilon$ model is widely used in nozzle flow simulations, its conventional formulation may limit prediction accuracy in confined geometries exhibiting strong anisotropic turbulence [26,42]. Therefore, the v^2-f turbulence model was adopted in conjunction with an automatic wall treatment. This combined approach complements the v^2-f model‘s improved capability in capturing anisotropic turbulence behavior within the narrow internal channels and complex stagnation regions near the substrate, while maintaining computational efficiency. This provides a robust prediction of gas-powder interactions without the strict necessity of fully resolving the viscous sublayer.

Mathematically, the underlying numerical solver implements the highly robust $\zeta-f$ model variant proposed by Hanjalić et al. [43] to circumvent the near-wall boundary singularity and numerical instability issues associated with the original Durbin framework [44]. Instead of solving directly for the wall-normal velocity fluctuations v^2, the implemented formulation solves transport equations for the turbulent kinetic energy, the turbulent dissipation rate, the normalized relative fluctuations $\zeta = v^2/k$, and an elliptic blending function that accounts for near-wall stress anisotropy.

Argon was used as the carrier, shielding, and shaping gas due to its inert nature and favorable density characteristics $\rho = 1.78$ kg/m³, $\mu = 2.09\times10^{-5}$ Pas. Based on the inlet conditions and nozzle geometry, the maximum gas velocity remained below 0.3 Ma throughout the domain; therefore, the flow was assumed incompressible.

A hybrid meshing strategy was employed to accurately resolve both the internal nozzle channels and the external flow domain.

The computational grid primarily consisted of tetrahedral elements supplemented with prism layers near wall regions and pyramid transition elements to improve mesh quality and boundary-layer resolution. Surface discretization was performed using triangular and quadrilateral elements.

To model the near-wall turbulence, an automatic wall treatment was applied. Given the macroscopic focus of the gas flow dynamics, this approach utilizes wall functions to accommodate the relatively coarse near-wall mesh, thereby ensuring an optimal balance between computational efficiency and the accurate prediction of bulk flow phenomena.

Considering the nozzle dimensions, flow conditions, and the establishment of fully developed flow near the exit region, stationary simulations were adopted to reduce computational cost while preserving the dominant flow characteristics.

The boundary conditions used in the numerical analysis are also illustrated in Fig. 4. The coaxial nozzle system includes the carrier gas inlet, shaping gas inlet, optical shielding gas inlet, exhaust outlets, and the main nozzle exit, all of which define the analysis boundaries.

For the simulations, the ambient temperature was set to $T_{ref} = 293.15$ K and the external atmospheric pressure to $P_{ref} = 1.0\times10^5$ Pa. All wall surfaces were assigned a no-slip condition. The 'suppress backflow' boundary condition was applied at the exit region to stabilize the interaction between the nozzle jet and the surrounding atmosphere. Initial simulations confirmed that this parameter has no significant impact on the powder flow dynamics within the convergence zone.

A unique data sampling strategy was implemented to determine the powder flow characteristics and the convergence zone with high precision. In conventional approaches, powder concentration is generally calculated using a plane perpendicular to the substrate [25,31]. While this method provides valuable insights, it essentially extracts linear (1D) data at each discrete height level, which may not fully capture spatial irregularities in a three-dimensional flow. Given the coaxial concentric nozzle used in this study, defining coaxial concentric circular counting areas parallel to the nozzle exit offers a more comprehensive 2D circular sampling approach. This strategy enables the dynamic monitoring of particle distribution and accounts for potential distortions in the coaxiality of the flow, ensuring a more holistic representation of the convergence behavior. As detailed in Fig. 5, three cylindrical subdomains with a diameter of 1.1 mm, matching the laser beam width, and a height of 1 mm were modeled consecutively at 1 mm intervals, extending from the substrate surface (Z=0) toward the nozzle exit. The bottom and top surfaces of these cylindrical volumes were utilized as data collection planes for particle counting, and these surfaces were called counting areas. This layered computational structure allows for high-precision tracking of the vertical distribution and mass concentration changes of powder particles within the critical region where they interact with the laser beam.

The color coding in Fig. 5 represents the dynamic progression of particles throughout the simulation. Red dots denote the particles that impact the upper counting area during the intermediate time steps of the simulation. Particles that have completed their transition through these upper areas and arrived at the substrate are displayed as green dots on the surface. However, the particles counted by the lowermost counting area, which is coincident with the substrate surface, are maintained as red. Blue dots represent the particles that did not come into contact with any of the counting areas during the flow and thus remained outside the measurement scope. By utilizing this methodology, the convergence density under different annular angles and gas flow rates was obtained with realistic data, enabling a comprehensive analysis of the spatial concentration and the specific level at which maximum convergence density occurs.

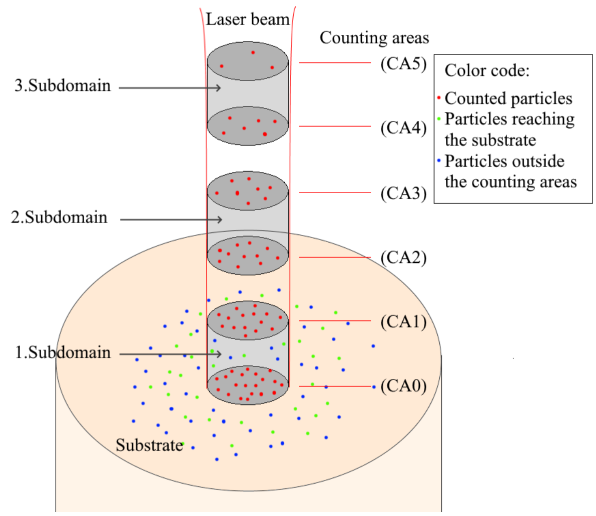

Fig. 5. Schematic representation of sampling subdomains and classification of particles by color based on plane interaction

2.3 Mesh Independence Study

A rigorous grid independence study was conducted to quantify the spatial discretization error and ensure that the numerical results are independent of the mesh resolution. The evaluation was performed following the grid convergence index (GCI) procedure outlined by Celik et al. [45]. Three different mesh configurations were utilized for the computational domain, as presented in Table 2 along with their respective skewness values to evaluate the mesh quality and the resulting response values in terms of average gas velocity taken from a plane at the nozzle outlet region. Each configuration maintained a mesh refinement ratio of $r > 1.3$.

The apparent order of convergence p was calculated to be 2.06, indicating monotonic convergence. Using a safety factor F_s of 1.25, the fine-grid convergence index GCI_{32} was determined to be 4.89 %, while the coarse-grid convergence index GCI_{21} was 9.94 %. The asymptotic ratio was calculated as 1.037, confirming that the numerical solutions are well within the asymptotic range of convergence.

Although the fine mesh provides the lowest discretization error, the relative error between the medium and fine mesh configurations was found to be sufficiently small $e_a^{32} = 3.76$ %. Therefore, to establish an optimal balance between high numerical fidelity and the significant computational resources required for complex, multiphase simulations, the medium mesh configuration $N_2 = 1.87\times10^6$ was selected for all subsequent analyses.

Table 2. Mesh independence study details

Mesh configuration	No. of elements	Average gas velocity [m/s]	Skewness
N_1	5.02×10^5	5.43	0.689
N_2	1.87×10^6	6.15	0.711
N_3	4.98×10^6	6.39	0.704

Following the grid independence verification, the established meshing strategy corresponding to the selected medium mesh configuration N_2 was applied to the specific geometries of both nozzle designs. Due to the different conical angle and the larger geometry needed to keep the flow channel lengths identical, maintaining the same mesh resolution naturally resulted in more elements for the narrow nozzle. Consequently, the narrow nozzle mesh comprised approximately 3.59×10^6 elements, while the wide nozzle mesh consisted of 1.87×10^6 elements. For both designs, the meshes achieved an average skewness quality of 0.7 and a minimum quality of 0.0025. These minimum quality elements were localized at the upper sections of the nozzle, specifically at the interfaces and intersection points of the nozzle components, well away from the critical flow regions and the nozzle exit, thereby ensuring that numerical accuracy was not compromised.

2.4 Powder Flow Visualization Technique

The numerical powder flow model was validated through a laser-assisted imaging technique to characterize the spatial intensity of the particle stream over the convergence zone. As shown in Fig. 6, a 5 mW line laser (650 nm) was aligned with the nozzle axis to illuminate the longitudinal cross-section of the coaxial flow cone.

Video sequences were recorded in frames per second (fps), at 60 fps for 3 seconds under stable conditions. To isolate the time-independent flow behavior, an intensity projection (temporal filtering) was applied to a stack of 180 frames. This statistical operator effectively suppressed stochastic particle fluctuations, yielding a high-contrast composite image of the stable flow boundaries. The resulting data served as a visual basis for evaluating the powder convergence zone against the CFD predictions. Figure 7 shows with and without intensity projection of an experiment.

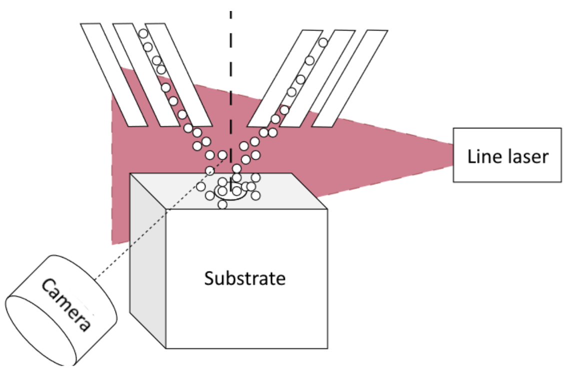

Fig. 6. Powder flow visualization technique

a)

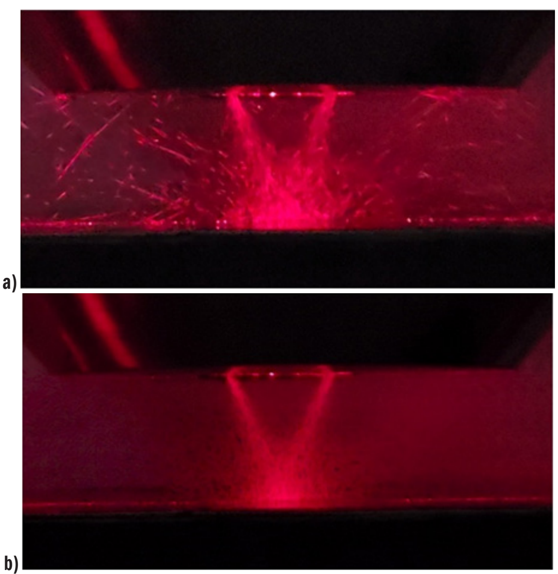

b)

Fig. 7. Comparison of images; a) without intensity projection, and b) with minimum intensity projection

3 RESULTS AND DISCUSSION

This section presents a comprehensive analysis of powder flow characteristics by integrating numerical CFD simulations with experimental flow visualization tests. To ensure the reliability of the computational framework, the powder stream morphology, convergence behavior, and focal stability were systematically validated against experimental observations. As summarized in Table 1, two nozzle configurations, narrow $\beta=24°$ and wide $\beta=35°$, were investigated under varying carrier and shaping gas velocities ranging from 4 m/s to 8 m/s. Unlike conventional free-jet approaches commonly reported in the literature, the explicit inclusion of a physical substrate positioned at a standoff distance of 10.85 mm enabled a realistic assessment of gas–surface interactions, including stagnation pressure formation, rebound mechanisms, and near-wall flow disturbances. By comparing numerical predictions with experimental results for each configuration (NN1–NN9 and WN1–WN9), the influence of gas velocity ratios and nozzle geometry on powder catchment efficiency and focus stability is discussed in detail.

Particle tracing analyses were conducted by quantifying the number of particles passing through predefined counting areas (CA), extending from the substrate surface (CA0) to the nozzle exit (CA5) as illustrated in Fig. 5. The ratios of particles traversing each level relative to the total injected powder mass were evaluated and are presented in Fig. 8 for the narrow nozzle (NN) and Fig. 9 for the wide nozzle (WN).

Particle counts above the CA3 level were negligible and therefore omitted from the analysis. The colored columns represent counting areas located at the planar surfaces of sub-volumes along the deposition axis and enable a direct comparison of particle transport efficiency across all nine operating conditions for each nozzle geometry. This quantitative framework provides a robust basis for correlating numerical predictions with experimental observations and for assessing the influence of gas flow parameters on particle delivery efficiency.

For the narrow nozzle configuration, the highest powder catchment efficiency at the CA0 level, defined as the theoretical convergence zone, was achieved in the NN4 condition, corresponding to a carrier gas flow rate of 9.5 L/min and shaping gas flow rate of 7.25 L/min (Fig. 8). A marginal decrease in efficiency was observed with increasing shaping gas flow rate, indicating that the carrier gas velocity is the dominant parameter governing powder transport in narrow nozzle geometries. This observation is consistent with previous studies reporting the primary role of carrier gas momentum in controlling particle trajectories and focal stability [25,46]. Notably, the peak efficiency in NN4 coincides with the condition where the carrier gas velocity at the orifice exit and the optical shielding gas velocity are identically matched at 6 m/s, complemented by a lower shaping gas velocity 4 m/s. This velocity alignment restricts the stagnation pressure zone on the substrate surface (Fig. 10a) and minimizes inter-layer velocity gradients between gas streams, thereby suppressing shear-induced dispersion and maintaining a well-focused stream of powder particles (Fig. 10c), in full agreement with the findings of [15]. Conversely, in NN3, which exhibits the lowest powder catchment efficiency at the CA0 level, a severe velocity mismatch occurs where the carrier gas velocity drops to a deficient 4 m/s, compounded by a significantly higher shaping gas velocity 8 m/s. This velocity variety induces highly complex, steep inter-layer gradients, which severely broaden the stagnation pressure zone on the substrate and creates an extended pressure barrier (Fig. 10b) that disrupts the laminar flow profile and scatters the powder trajectories (Fig. 10d).

To put these findings into perspective, a similar analysis was conducted for the wide nozzle configuration (Fig. 11). In contrast to

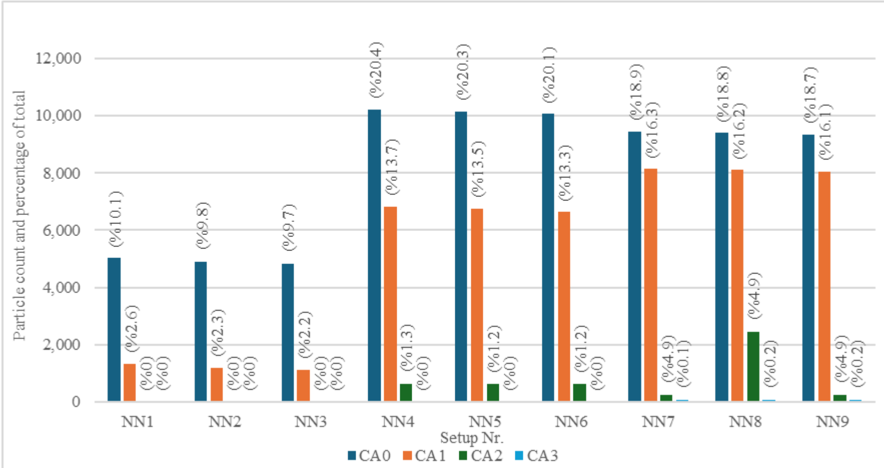

Fig. 8. Particle counts and relative percentages within the counting area of the narrow nozzle

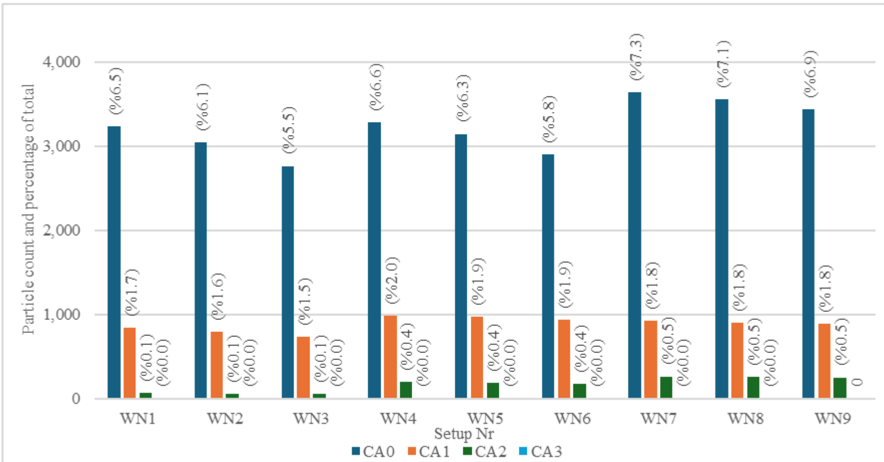

Fig. 9. Particle counts and relative percentages within the counting area of the Wide Nozzle

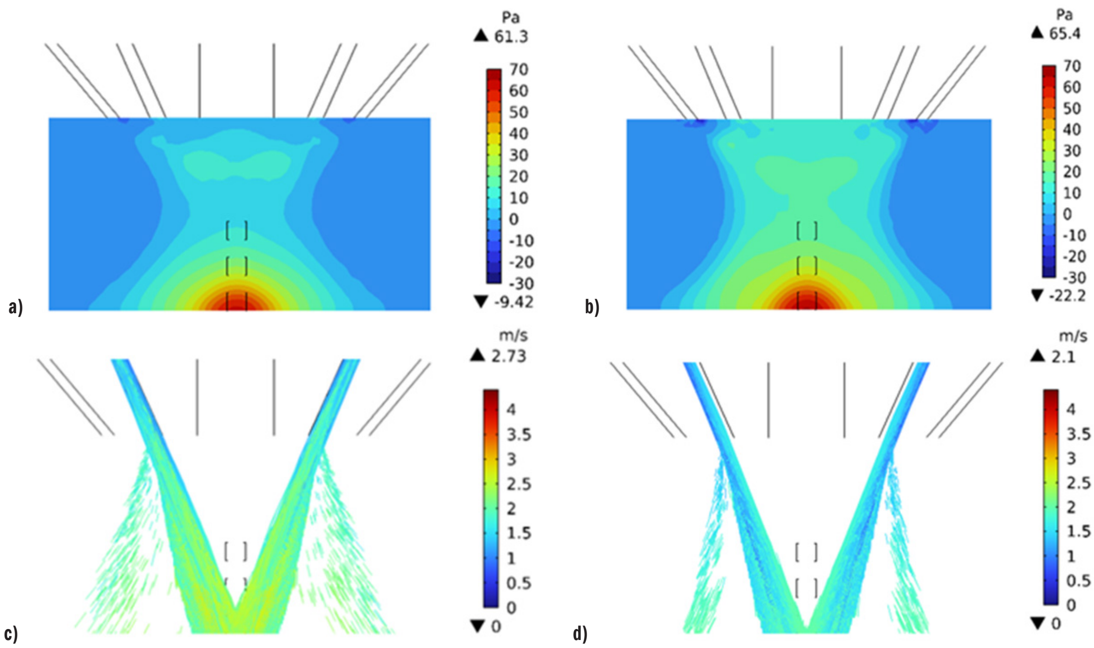

Fig. 10. Narrow nozzle at: a) NN4 pressure profile, b) NN3 pressure profile, c) NN4 particle trajectories, and d) NN3 particle trajectories

the narrow configuration, the wide nozzle configuration exhibited only minor variations in particle distribution across the investigated gas flow rates, resulting in closely clustered efficiency values. Although a general tendency toward increased catchment efficiency

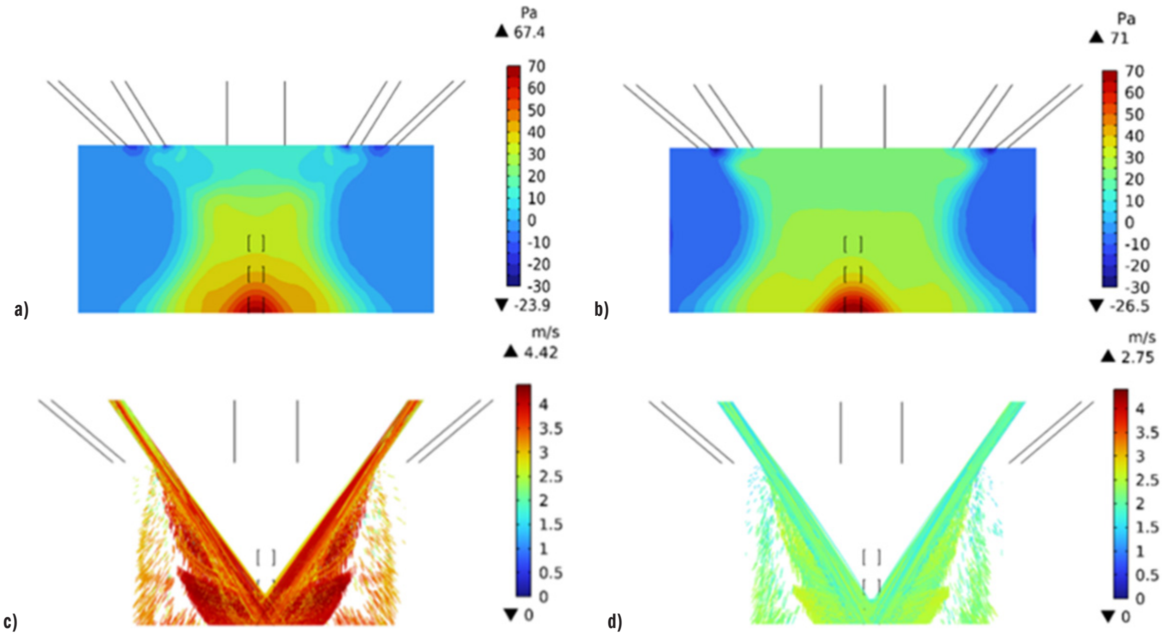

Fig. 11. Wide nozzle at: a) WN7 pressure profile, b) WN3 pressure profile, c) WN7 particle trajectories, and d) WN3 particle trajectories

with higher carrier gas velocity and reduced efficiency with increasing shaping gas velocity was observed in the narrow nozzle, these effects remained marginal and did not constitute a decisive factor for the wide nozzle geometry. This behavior can be attributed to the dilution of momentum transfer over a larger interaction volume, where flow streamlines remain farther from the central axis, reducing the sensitivity of particle convergence to gas velocity variations [24]. Compared to the narrow nozzle configuration, the wide nozzle achieved less than one-third of the peak efficiency, marking it as a less suitable design for high-performance applications. This substantial disparity underscores the inefficiency of the wide geometry in powder convergence. Consequently, due to its poor material utilization and sub-optimal flow characteristics (Fig. 11), the wide nozzle is considered an unfavorable design and is therefore not recommended for high-efficiency laser metal deposition applications within the investigated parameter range.

Regarding the role of the shaping gas, the results clearly indicate that its influence on powder convergence is secondary to that of the carrier gas. More importantly, increasing the shaping gas flow rate beyond a critical threshold leads to a reduction in catchment efficiency in both nozzle geometries. This suggests that an excessive shaping gas velocity disrupts the laminar flow profile by inducing high shear-related turbulence between gas layers. Furthermore, higher shaping gas rates contribute to the expansion of the stagnation pressure zone above the substrate, which effectively repels low-momentum particles from the central axis. A similar particle-deflection mechanism has been reported in CFD-based investigations of gas-particle impinging flows, where the stagnation zone formed near the target surface was shown to decelerate the flow and induce lateral deflection of entrained particles, thereby altering their trajectories and effective momentum transfer [47]. Consequently, employing a lower shaping gas flow rate, ideally just enough to maintain the powder stream's integrity, is a more strategic approach to maintain focal stability and minimize aerodynamic resistance.

Detailed pressure contours of both nozzles (Figs. 12 and 13) reveal that deposition efficiency is fundamentally governed by the spatial distribution of the gas pressure field. High-efficiency conditions (NN4 and WN7) are characterized by a confined high-pressure zone around the substrate and a well-balanced velocity distribution along the deposition axis (Fig. 12a and 13a). In contrast, low-efficiency conditions (NN3 and WN3) exhibit an expanded pressure field, which acts as a stagnation barrier that restricts particle penetration toward the convergence area. For instance, in the wide nozzle configuration, the average pressure in the convergence zone was higher for the relatively less efficient WN3 condition (71 Pa) compared to the more efficient WN7 case (67.4 Pa). Similarly, in the narrow nozzle configuration, the average pressure was higher for the less efficient NN3 condition (72.5 Pa) compared to the NN4 case (68.8 Pa).

While the stagnation pressure field plays a critical role within each respective nozzle design, a cross-comparison between the two configurations highlights the inherent geometric superiority of the narrow nozzle. Efficiency results (Figs. 8 and 9) demonstrate

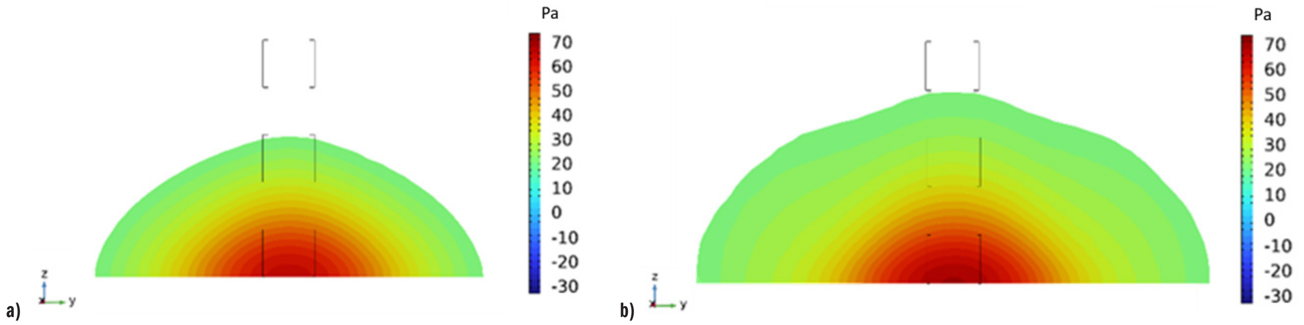

Fig. 12. Narrow nozzle; a detailed pressure profiles: a) NN4, and b) NN3

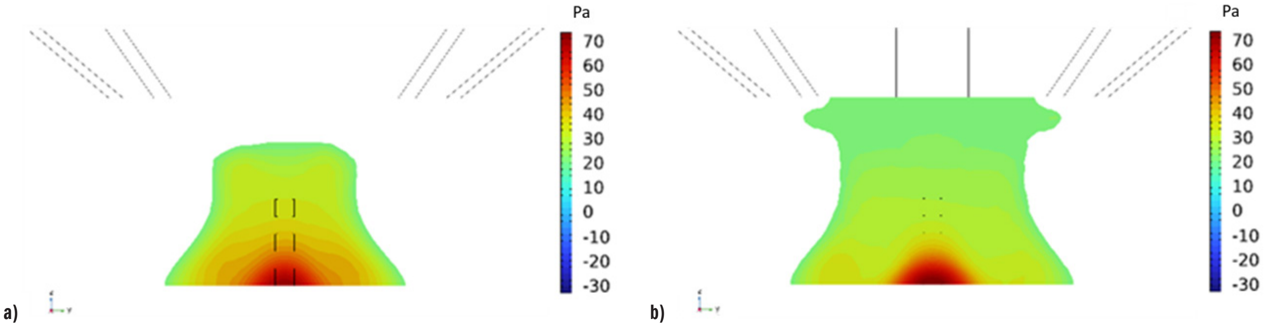

Fig. 13. Wide nozzle; detailed pressure profiles: a) WN7, and b) WN3

that the narrow nozzle is significantly more effective, with even its less efficient condition (NN3) outperforming the most optimized wide nozzle case (WN7), despite NN3 exhibiting a higher absolute stagnation pressure (72.5 Pa) than WN7 (67.4 Pa), thereby proving that geometric particle confinement dominates over absolute pressure resistance. As observed in the velocity magnitude scales and trajectory plots (Figs. 10 and 11), although the wide nozzle (WN7) operates at higher localized velocity scales near the peripheral walls, it fails to maintain a focused axial stream due to the velocity-induced momentum dilution. In contrast, the narrow nozzle (NN4) exhibits a superior focal concentration, keeping the particles within a much tighter flow path along the central axis. Furthermore, a closer inspection of these velocity fields indicates that the peak powder concentration along the focal line occurs precisely in regions where particle velocity reaches a local minimum. This behavior highlights the critical balance between aerodynamic drag and particle inertia, where the localized deceleration of particles facilitates a denser accumulation along the central stream. This indicates that the narrow nozzle geometry is more successful at preventing lateral particle dispersion, regardless of the initial velocity parameters.

In both designs, as the pressure field expands, particles deviate from the flow axis due to loss of axial momentum and trajectory deviations (Figs. 10d and 11d). This forces particles into peripheral flow paths, particularly affecting low-momentum particles and leading to reduced focal concentration, a mechanism consistent with findings reported in previous studies [24,38,48].

The explicit inclusion of the substrate in the gas flow simulations revealed the formation of dominant toroidal vortices and turbulence structures generated by jet impingement on the surface. These vortical structures disrupt powder focusing and can entrap low-momentum particles, a phenomenon not captured by substrate-free jet models commonly used in the literature [38,49,50]. For reference, preliminary substrate-free baseline gas flow simulations were also performed. In these free-jet cases, the pressure field remained essentially uniform, and streamlines of the gas flow progressed axially without evidence of dominant toroidal vortices or a localized positive stagnation pressure at an impingement surface. By contrast, substrate-induced simulations, performed under the same parameter settings as the substrate-free cases, consistently produced a localized positive stagnation pressure at the impingement region and clear dominant toroidal vortex structures, which induced an upward shift of the powder focal point toward the nozzle exit. Gas flow streamlines and pressure profiles of the substrate-free and substrate-induced cases are shown overlaid in Figs. 14a and b, respectively. This rebound-driven stagnation and vortex formation directly affect deposition efficiency and are therefore often underestimated or entirely neglected in simplified simulations [24,38]. Their explicit inclusion is necessary to correctly predict powder focusing behavior and to guide design-oriented optimization.

From a turbulence modeling perspective, the $v^2\!-\!f$ turbulence model was implemented in this study to capture anisotropic turbulence and complex near-wall boundary layer effects within the narrow annular channels of the nozzle. While standard $k\!-\!\varepsilon$ models have been widely used in the literature [15], our simulation results show that the near-wall velocity variance (ζ) and elliptic blending (α) effects adequately represent the complex flow physics of the focal zone [17]. Utilizing this formulation alongside an automatic wall treatment allowed for consistent tracking of particle exit trajectories and convergence behavior, without necessitating the prohibitive computational cost of directly resolving the viscous sublayer.

In alignment with literature models [41,51], accounting for the bidirectionally coupled (2-way) interaction, where the gas stream is forced to bend around zones of high particle concentration, enables an accurate determination of the convergence efficiency for the narrow nozzle geometry investigated in this study.

The number density distributions for the selected high- and low-efficiency conditions clearly illustrate the effect of nozzle geometry and gas flow configuration on powder focusing behavior (Figs. 15 and 16). In the narrow nozzle, the high-efficiency NN4 condition exhibits a compact and axisymmetric high-density core concentrated along

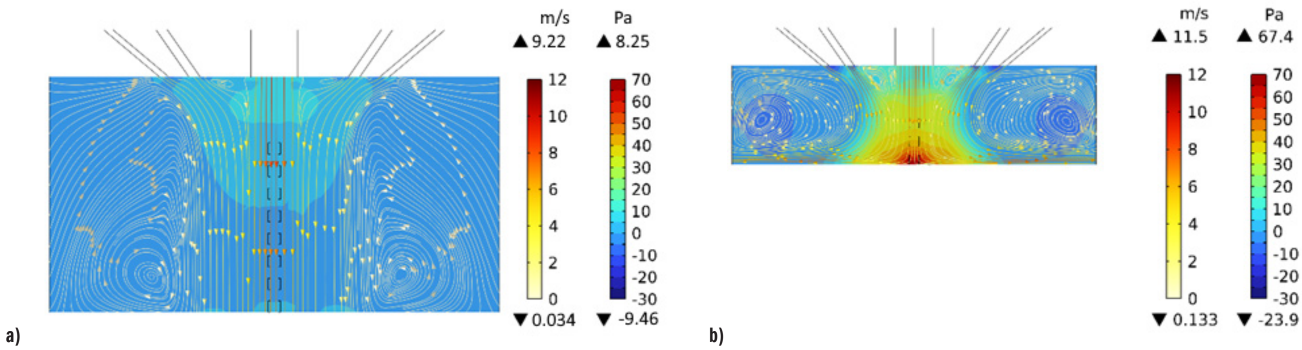

Fig. 14. Streamlines and pressure profiles: a) substratefree case, and b) substrateinduced case

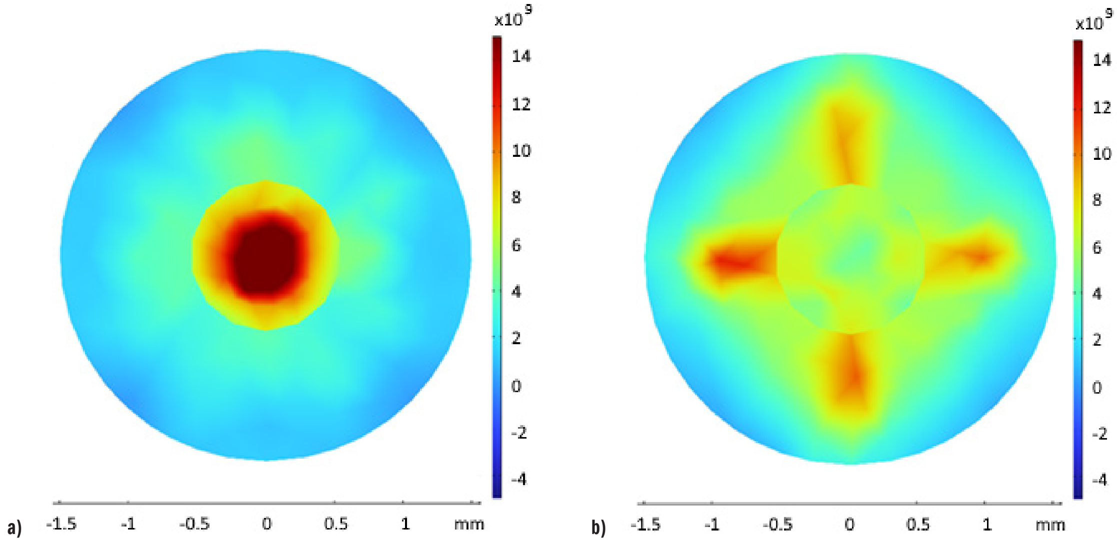

Fig. 15. Narrow nozzle – number density: a) NN4, and b) NN3

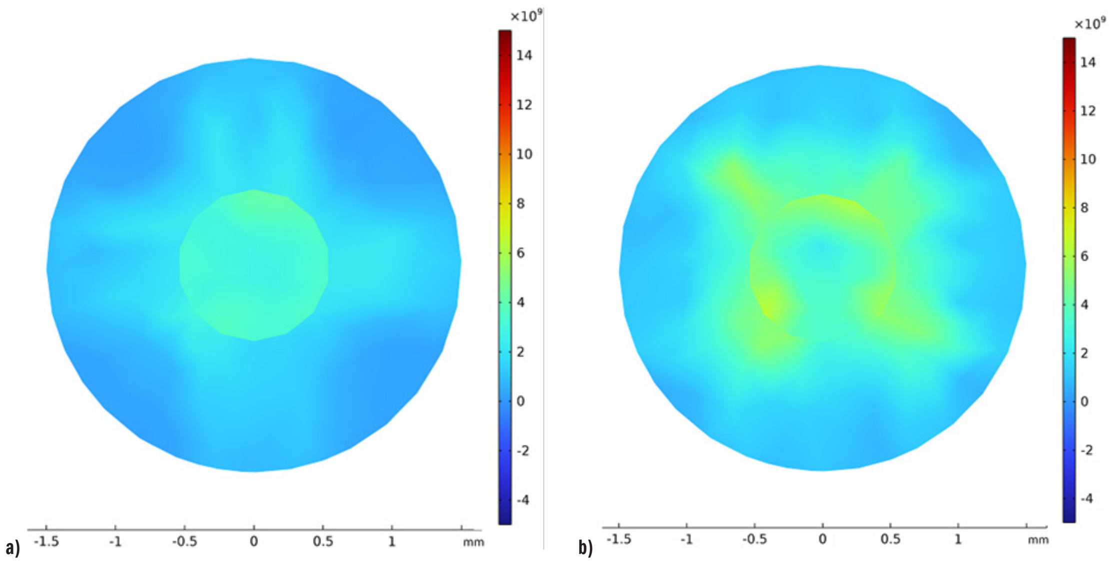

Fig. 16. Wide nozzle – number density; a) WN7, and b) WN3

the central axis, indicating effective particle convergence within the focal region (Fig. 15a). In contrast, the low-efficiency NN3 condition shows a fragmented and off-axis density distribution, reflecting disrupted axial transport and increased peripheral dispersion (Fig. 15b). For the wide nozzle, even the most efficient case (WN7) presents a lower and more diffuse central density compared to the narrow nozzle, while the low-efficiency WN3 condition demonstrates a further loss of focal coherence with asymmetric density patterns (Fig. 16a and 16b). Overall, these results indicate that a compact, centrally concentrated number density distribution is a key indicator of high powder catchment efficiency, whereas dispersed or lobed patterns correspond to defocused flow regimes.

The narrow nozzle (β=24°) exhibited a markedly higher sensitivity to gas flow variations and substrate-induced pressure changes than the wide nozzle. This finding confirms that while small-angle nozzles offer significantly higher peak efficiencies, they demand precise parameter optimization to maintain a stable powder focus, as previously reported by [10,24]. In contrast, the wide nozzle configuration demonstrated reduced sensitivity due to the broader spatial distribution of momentum transfer. The Ti6Al4V powder used in this study (mean particle size ≈ 90 µm) exhibited optimal aerodynamic behavior at a velocity matching condition of 6 m/s, resulting in a higher catchment efficiency compared to the other investigated conditions.

Experimental flow visualization images for the maximum and minimum efficiency cases are presented alongside the corresponding numerical particle velocity contours in Figs. 17 and 18 for narrow and wide nozzles, respectively. The characteristic convergence morphology of the powder stream post-nozzle exit demonstrates a good qualitative agreement between the numerical model prediction and the experimental camera observations. A direct visual comparison between the two nozzle designs highlights the clear superiority of the narrow nozzle in achieving a more concentrated particle stream within the focal area. The macroscopic shape of the convergence zone and the visually observable stagnation effect in the experiments physically align with the numerical velocity fields. This morphological consistency provides qualitative confidence in the model's ability to capture the underlying flow physics, supporting the conclusion that NN4 is the optimal configuration for powder catchment efficiency.

Finally, while the direct numerical modeling of melt pool dynamics falls outside the scope of this study, understanding the gas velocity

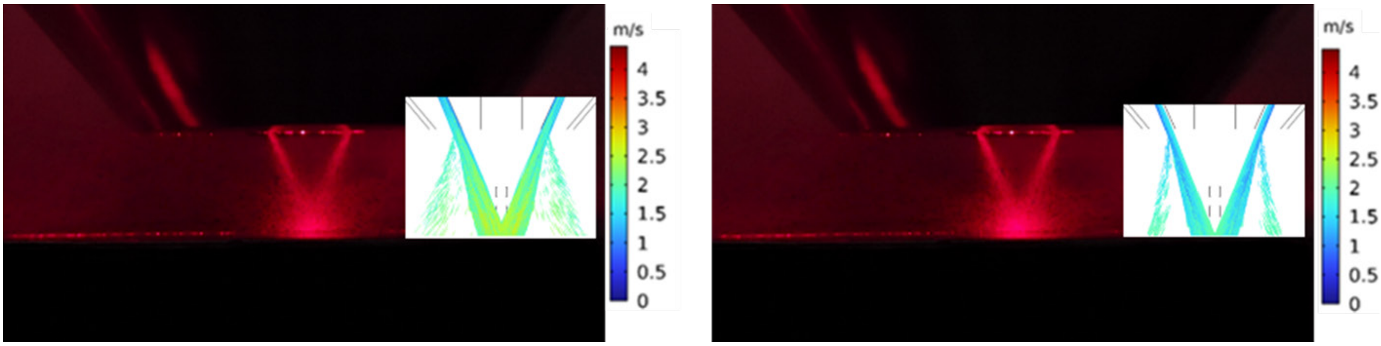

a) b)

Fig. 17. Narrow Nozzle experimental particle flow visualization; a) NN4, and b) NN3

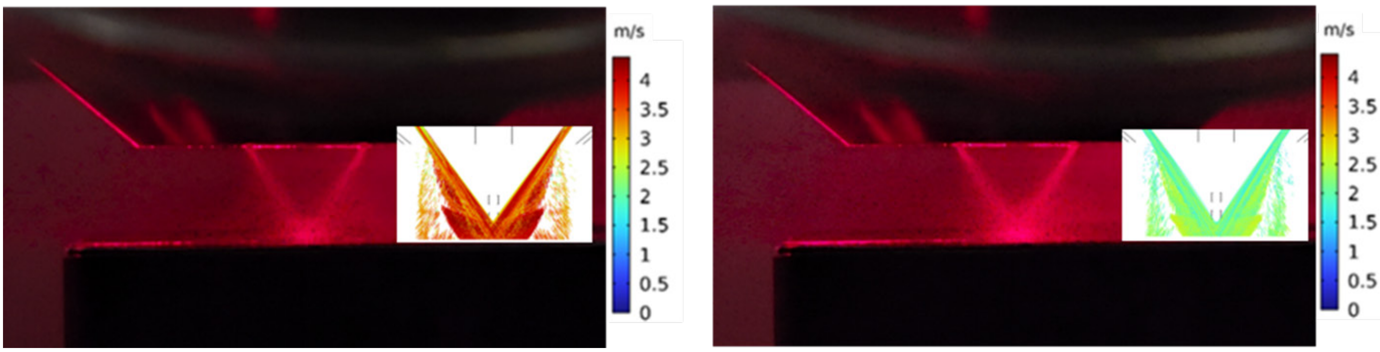

a) b)

Fig. 18. Wide nozzle experimental particle flow visualization; a) WN7, and b) WN3

distributions provides valuable insight into the physical conditions governing the deposition process. Previous studies have demonstrated that excessively high carrier gas velocities, although beneficial for particle transport, can adversely affect melt pool behavior by accelerating cooling, reducing melt pool dimensions, increasing the likelihood of gas entrapment–induced porosity, destabilizing laminar surface flow through intense particle impingement, and promoting spatter formation [31,52]. Therefore, evaluating the gas velocity field is important not only for understanding powder transport but also for assessing process conditions that may influence melt pool stability and deposition quality. In this context, our findings regarding the velocity fields, together with the incorporation of powder–gas interactions through two-way coupling, provide a physically meaningful basis for interpreting the deposition efficiency losses observed in narrow nozzle geometries and their potential relationship with the gas-flow-induced phenomena reported in the literature [41].

Overall, these results demonstrate that the optimization of gas flow rates is a critical parameter for stabilizing the flow regime and effectively directing particles into the convergence zone. The impact of gas flow rates on pressure and velocity distributions is strongly dependent on nozzle inclination angle and the resulting geometric variation in the orifice exit area. This structural dependency underscores the necessity of geometry-specific parameter optimization to maximize powder catchment efficiency and ensure focal stability in directed energy deposition processes.

4 CONCLUSIONS

This study presents a design-based assessment of continuous coaxial DED nozzles by systematically evaluating the influence of nozzle geometry and gas flow interactions under realistic deposition conditions. Unlike conventional free-jet models, the explicit inclusion of a physical substrate revealed critical substrate-induced flow phenomena—such as stagnation pressure formation, rebound mechanisms, and near-wall vortical structures—that strongly govern powder convergence behavior and material utilization.

The comparative analysis of narrow (β=24°) and wide (β=35°) nozzle geometries demonstrated that nozzle inclination plays a decisive role in controlling powder focusing through its effect on momentum transfer and pressure field distribution. The narrow nozzle consistently produced a compact, axisymmetric powder stream with significantly higher catchment efficiency, whereas the wide nozzle exhibited diffuse flow patterns and pronounced sensitivity to pressure expansion, resulting in substantial particle dispersion. These differences persisted across all investigated gas velocity combinations, indicating that geometric configuration is a dominant design parameter relative to gas flow rate variations.

The results further show that carrier gas momentum governs axial particle transport, while excessive shaping gas velocity adversely affects convergence by inducing shear-driven turbulence and enlarging the stagnation pressure zone above the substrate. Velocity matching between the carrier gas and optical shielding gas was identified as a favorable condition for stabilizing the flow field and minimizing inter-layer velocity gradients, thereby promoting a stable convergence regime. Number density analyses corroborated these findings by demonstrating that high-efficiency conditions are characterized by a dense, centrally concentrated particle core, whereas low-efficiency cases exhibit fragmented or off-axis density distributions.

From a modeling perspective, the use of a v^2–f turbulence formulation combined with two-way powder–gas coupling proved essential for accurately resolving near-wall effects and momentum exchange in narrow annular channels. The simulations confirmed that powder–gas feedback significantly alters the local flow field in the focal region, further emphasizing the limitations of simplified substrate-free approaches that fail to capture substrate-induced stagnation pressures and near-wall vortical structures.

Overall, this work does not propose an optimized nozzle design but rather provides a physics-based framework for selecting and evaluating continuous coaxial nozzle geometries based on gas flow interactions and substrate-induced effects. The findings offer practical design guidance for DED nozzle selection, highlighting the necessity of geometry-specific parameter tuning and realistic boundary condition modeling to achieve stable powder convergence and efficient material utilization.

References

[1] Calik, B., Uzun, G. Applications of topology optimization in metal additive manufacturing. *Gazi Uni Inst Sci Technol C: Design Technol 12* 832-844 (2024) **DOI:10.29109/gujsc.1542929**. (in Turkish)

[2] Arrizubieta, J.I., Ruiz, J.E., Martinez, S., Ukar, E., Lamikiz, A. Intelligent nozzle design for the laser metal deposition process in the Industry 4.0. *Proc Manuf 13* 1237-1244 (2017) **DOI:10.1016/j.promfg.2017.09.043**.

[3] Iftekar, S.F., Aabid, A., Amir, A., Baig, M. Advancements and limitations in 3D printing materials and technologies: A critical review. *Polymers 15* 11 (2023) **DOI:10.3390/polym15112519**.

[4] Güler, S., Serindag, H. T., Çam, G. Wire arc additive manufacturing (WAAM): Recent developments and prospects. *Eng Machins 63* 82-116 (2022) **DOI:10.46399/muhendismakina.995979**.

[5] Cho, K.T., Nunez, L., Shelton, J., Sciammarella, F. Investigation of effect of processing parameters for direct energy deposition additive manufacturing technologies. *J Manuf Mater Process 7* 105 (2023) **DOI:10.3390/jmmp7030105**.

[6] Thompson, S.M., Bian, L., Shamsaei, N., Yadollahi, A. An overview of direct laser deposition for additive manufacturing; Part I: Transport phenomena, modeling and diagnostics. *Addit Manuf 8* 36-62 (2015) **DOI:10.1016/j.addma.2015.07.001**.

[7] Zhou, Y., Hiang, D., Al-Akalilah, A., Ning, F. Understanding the formation of laser-induced melt pools with both wire and powder feeding in directed energy deposition. *Addit Manuf 89* 104312 (2024) **DOI:10.1016/j.addma.2024.104312**.

[8] Kumar, S.P., Elangovan, S., Mohanraj, R., Srihari, B. Critical review of off-axial nozzle and coaxial nozzle for powder metal deposition. *Mater Today Proc 46* 8066-8079 (2021) **DOI:10.1016/j.matpr.2021.03.037**.

[9] Singh, A., Kapil, S., Das, M. A comprehensive review of the methods and mechanisms for powder feedstock handling in directed energy deposition. *Addit Manuf 35* 11388 (2020) **DOI:10.1016/j.addma.2020.101388**.

[10] Gabor, T., Yun, H., Akin, S., Kim, K.H., Park, J.K., Jun, M.B.G. Continuous coaxial nozzle designs for improved powder focusing in direct laser metal deposition. *J Manuf Proc 83* 116-128 (2022) **DOI:10.1016/j.jmapro.2022.08.039**.

[11] Guner, A., Bidare, P., Jimenez, A., Dimov, S., Essa, K. Nozzle designs in powderbased direct laser deposition: A review. *Int J Prec Eng Manuf 23* 1077-1094 (2022) **DOI:10.1007/s12541-022-00688-1**.

[12] Nasiri, M.T., Movahhedy, M.R. A new design of continuous coaxial nozzle for direct metal deposition process to overcome the gravity effect. *Prog Addit Manuf 7* 173-186 (2022) **DOI:10.1007/s40964-021-00223-0**.

[13] Govekar, E., Jeromen, A., Kuznetsov, A., Kotar, M., Kondo, M. Annular laser beam based direct metal deposition. *Proc CIRP 74* 222-227 (2018) **DOI:10.1016/j.procir.2018.08.099**.

[14] Mousa, M., Osman, H., Azab, A., El-Gaddar, A., Baki, F. Characterization of laser cladding functional coatings: an in-situ monitoring and variability analysis approach. *Int J Adv Manuf Technol 133* 1155-1183 (2024) **DOI:10.1007/s00170-024-13764-9**.

[15] Ferreira, E., Dal, M., Peyre, P., Colin, C., Marion, G., Courapied, D., et al. Numerical and experimental investigation of gas powder flow from coaxial nozzles in laser metal deposition. *Proc COMSOL Conf* (2018).

[16] Ermurat, M, Arslan, M.A., Erzincanli, F., Uzman, I. Process parameters investigation of a laser-generated single clad for minimum size using design of experiments. *Rapid Prototyp J 19* 452-462 (2013) **DOI:10.1108/RPJ-06-2011-0062**.

[17] Chai, Q., He, X., Xing, Y., Sun, G. Numerical study on the collision effect of particles in the gas-powder flow by coaxial nozzles for laser cladding. *Optic Laser Tech 163* 109449 (2023) **DOI:10.1016/j.optlastec.2023.109449**.

[18] Zhang, B., Coddet, C. Numerical study on the effect of pressure and nozzle dimension on particle distribution and velocity in laser cladding under vacuum base on CFD. *Manuf Proc 23* 54-60 (2016) **DOI:10.1016/j.jmapro.2016.05.019**.

[19] Morville, S., Carin, M., Carron, D., Le Masson, P., Gharbi, M., Peyre, P., Fabbro, R. Numerical modeling of powder flow during coaxial laser direct metal deposition - comparison between Ti-6Al-4V alloy and stainless steel 316L. *Proc COMSOL Conference* (2012).

[20] Arrizubieta, J.I., Tabernero, I., Ruiz, J.E., Lamikiz, A., Martinez, S., Ukar, E. Continious coaxial nozzle design for LMD based on numerical simulation. *Physics Proc* 429-438 (2014) **DOI:10.1016/j.phpro.2014.08.146**.

[21] Tozue, S., Rauch, M., Hascoet, J.-Y. Gas-particle flow of cohesive aluminum powders during laser metal deposition - Experimental and numerical investigation. *Adv Powder Tech 34* 104182 (2023) **DOI:10.1016/j.apt.2023.104182**.

[22] Nogdhe, Y., Rai, A.K., Manjaiah, M. Numerical study of powder flow characteristics of coaxial nozzle direct energy deposition at different operating and design conditions. *Progr Addit Manuf 10* 701-723 (2025) **DOI:10.1007/s40964-024-00652-7**.

[23] Liu, Q., Yang, K., Gao, Y., Liu, F., Huang, C., Ke, L. Analytical study of powder stream geometry in laser-based direct energy deposition process with a continuous coaxial nozzle. *Crystals 11* 1306 (2021) **DOI:10.3390/cryst11111306**.

[24] Martínez A.L. Ibarra-Medina, J., García-Moreno, A.I., Piedra, S:, Vizcaya, L.L., Martínez-Franco, E., et al, Modeling and comparison of the powder flow dynamics for tilted annular and discrete-outlet nozzles in laser directed energy deposition. *J Manuf Proc 99* 687-704 (2023) **DOI:10.1016/j.jmapro.2023.05.039**.

[25] Guan, X., Zhao, Y.F. (2020). Numerical modeling of coaxial powder stream in laser-powder-based directed energy deposition process. *Addit Manuf 34* 101226 (2020) **DOI:10.1016/j.addma.2020.101226**.

[26] Gao, J., Wu, C., Liang, X., Hao, Y., Zhao, K. Numerical simulation and experimental investigation of the influence of process parameters on gas-powder flow in laser metal deposition. *Opt Laser Tech 125* 106009 (2020) **DOI:10.1016/j.optlastec.2019.106009**.

[27] Wu, J., Zhao, P., Wei, H., Lin, Q., Zhang, Y. Development of powder distribution model of discontinuous coaxial powder stream in laser direct metal deposition. *Powder Tech 340* 449-458 (2018) **DOI:10.1016/j.powtec.2018.09.032**.

[28] Lalas, C., Tsirbas, K., Salonitis, K., Chryssolouris, G. An analytical model of the laser clad geometry. *Int J Adv Manuf Technol 32* 34-41 (2007) **DOI:10.1007/s00170-005-0318-0**.

[29] Liu, S., Kovacevic, R. Numerical Simulation and experimental study of powder flow distribution in high power direct diode laser cladding process. *Laser Manuf Mater Proc 2* 199-218 (2015) **DOI:10.1007/s40516-015-0015-2**.

[30] Balu, P., Leggett, P., Kovacevic, R. Parametric study on a coaxial multi-material powder flow in laser-based powder deposition process. *J Material Proc Tech 212* 1598-1610 (2012) **DOI:10.1016/j.jmatprotec.2012.02.020**.

[31] Takemura, S., Koike, R., Kakinuma, Y., Sato, Y., Oda, Y. Design of powder nozzle for high resource efficiency in directed energy deposition based on computational fluid dynamics simulation. *Int J Adv Manuf Tech 105* 4107-4121 (2019) **DOI:10.1007/s00170-019-03552-1**.

[32] Yao, X.X., Li, J.Y., Wang, Y.F., Gao, X., Li, T., Zhang, Z. Experimental and numerical studies of nozzle effect on powder flow behaviors in directed energy deposition additive manufacturing. *Int J Mech Sci 210* 106740 (2021) **DOI:10.1016/j.ijmecsci.2021.106740**.

[33] Tabernero, I., Lamikiz, A., Ukar, E., Lacalle, L.L., Angullo, C., Urbikain, G. Numerical simulation and experimental validation of powder flux distribution in coaxial laser cladding. *J Mater Process Technol 210* 2125-2134 (2010) **DOI:10.1016/j.jmatprotec.2010.07.036**.

[34] Liu, H., Hao, J., Yu, G., Yang, H.F., Wang, L.W. Han, Z.T. A numerical study on metallic powder flow in coaxial laser cladding. *J Appl Fluid Mech 9* 2247-2256 (2016) **DOI:10.18869/acadpub.jafm.68.236.25632**.

[35] Kovaleva, I., Kovalev, O., Zaitsev, A.V., Sergachev, D.V. Modeling and numerical study of light-propulsion phenomena of particles acceleration in coaxial laser powder cladding. *Phys Procedia 56* 439-449 (2014) **DOI:10.1016/j.phpro.2014.08.147**.

[36] Xia, Y., Huang, Z., Chen, H., Liang, X., Lei, J. Numerical simulation and experimental investigation on powder transport of a new-type annular coaxial nozzle. *Int J Adv Manuf Technol 115* 2353-2364 (2021) **DOI:10.1007/s00170-021-07294-x**.

[37] Grass Nunez, J.S., Rojas Perilla, D.A., Barragan De Los Ríos, G.A., Coelho, R.T. Numerical and experimental analysis of gas flow in a coaxial nozzle applied to directed energy deposition (DED). *Int J Eng Mater Manuf 6* 102-113 (2021) **DOI:10.26776/ijemm.06.03.2021.01**.

[38] Ibarra-Medina, J., Pinkerton, A.J., A CFD model of the laser, coaxial powder stream and substrate interaction in laser cladding. *Phys Proc 5* 337-346 (2010) **DOI:10.1016/j.phpro.2010.08.060**.

[39] Mazzucato, F., Tusacciu, S., Lai, M., Biamino, S., Lombardi, M., Valente, A. Monitoring approach to evaluate the performances of a new deposition

nozzle solution for DED systems. *Technologies 5* 29 (2017) **DOI:10.3390/technologies5020029**.

[40] Guan, X., Zhao, Y.F. Modeling of the laser powder-based directed energy deposition process for additive manufacturing: a review. *Int J Adv Manuf Technol 107* 1959-1982 (2020) **DOI:10.1007/s00170-020-05027-0**.

[41] Bedenko, D.V., Kovalev, O.B., Sergachev, D.V. Numerical study of the gas-particle flows with the two-way coupling formed by coaxial nozzles for laser cladding. *Surface Coat Technol 445* 12870 (2022) **DOI:10.1016/j.surfcoat.2022.128700**.

[42] Khamidullin, B.A., Tsivilskiy, I.V., Gorunov, A.I., Gilmutdinov, A.K. Modeling of the effect of powder parameters on laser cladding using coaxial nozzle. *Surface Coat Technol 364* 430-443 (2019) **DOI:10.1016/j.surfcoat.2018.12.002**.

[43] Hanjalić, K., Popovac, M., Hadžiabdić, M. A robust near-wall elliptic-relaxation eddy-viscosity turbulence model for CFD. *Int J Heat Fluid Flow 25* 1047-1051 (2004) **DOI:10.1016/j.ijheatfluidflow.2004.07.005**.

[44] Durbin, P.A., Near-wall turbulence closure modeling without ‚damping functions'. *Theoret Comput Fluid Dyn 3* 1-13 (1991) **DOI:10.1007/BF00271513**.

[45] Celik, I.B., Ghia, U., Roache, P.J., Freitas, C.J. Procedure for estimation and reporting of uncertainty due to discretization in CFD applications. *J Fluid Eng 130* 078001 (2008) **DOI:10.1115/1.2960953**.

[46] Li, B., Wang, W., Li, D., Liu, Z., Ren, Y., Wang, Y., et al. The influence of the annular nozzle's structural parameters on powder stream convergence for laser-directed energy deposition. *Materials 18* 2055 (2025) **DOI:10.3390/ma18092055**.

[47] Yuan, Y., Wang, J., Chen, J., Yu, Y., Xie, Y., Wang, H., et al. Exploration of erosion characteristics in multi-step machining by CFD-assisted abrasive waterjet. *Stroj vest-J Mech E 72* 144-157 (2026) **DOI:10.5545/sv-jme.2025.1597**.

[48] Nagulin, K.Y., Iskhakov, F.R., Shpilev, A.I., Gilmutdinov, A.Kh. Optical diagnostics and optimization of the gas-powder flow in the nozzles for laser cladding. *Optic Laser Technol 108* 310-320 (2018) **DOI:10.1016/j.optlastec.2018.07.001**.

[49] Zekovic, S., Dwivedi, R., Kovacevic, R. Numerical simulation and experimental investigation of gas-powder flow from radially symmetrical nozzles in laser-based direct metal deposition. *Int J Mach Tool Manuf 47* 112-123 (2007) **DOI:10.1016/j.ijmachtools.2006.02.004**.

[50] Kovalev. O.B., Bedenko, D.V., Zaitsev, A.V. Development and application of laser cladding modeling technique: From coaxial powder feeding to surface deposition and bead formation. *App Math Model 57* 339-359 (2018) **DOI:10.1016/j.apm.2017.09.043**.

[51] Bian, Y., He, X., Yu, G., Li, S., Tian, C., Li, Z., et al. Powder-flow behavior and process mechanism in laser directed energy deposition based on determined restitution coefficient from inverse modeling. *Powder Technol 402* 117355 (2022) **DOI:10.1016/j.powtec.2022.117355**.

[52] Wirth, F., Arpagaus, S., Wegener, K. Analysis of melt pool dynamics in laser cladding and direct metal deposition by automated high-speed camera image evaluation. *Addit Manuf 21* 369-382 (2018) **DOI:10.1016/j.addma.2018.03.025**.

Acknowledgements *This research was funded by TUBITAK, grant number 123M045. We also acknowledged to the Turkish distributor, Eti Bilgisayar Ltd. Sti., for providing the academic trial license of COMSOL Multiphysics software.*

Received *2026-02-04* **revised***: 2026-05-21, 2026-06-26,* **accepted***: 2026-08-19 as original scientific paper.*

Data Availability *The data presented in this study are available on request from the corresponding author.*

Author Contribution *Mehmet Ermurat: Conceptualization, Methodology, Validation, Formal Analysis, Investigation, Resources, Data Curation, Writing—Original Draft Preparation, Writing—Review and Editing, Visualization, Supervision, Project Administration, Funding Acquisition; Muhammet Ibrahim Asci: Methodology, Software, Validation, Formal Analysis, Investigation, Visualization; Ibrahim Hakki Ince: Methodology, Software, Formal Analysis, Investigation, Visualization. All authors have read and agreed to the published version of the manuscript.*

Ocena zasnove zveznih koaksialnih šob za DED z upoštevanjem vpliva substrata na tok plina

Povzetek *Zvezne koaksialne šobe se pogosto uporabljajo pri usmerjenem nanašanju materiala (DED), vendar številne numerične raziskave temeljijo na modelih prostega curka brez substrata, ki ne zajamejo ključnih interakcij med plinom in površino. Ta študija zajema raziskavo zasnove zvezne koaksialne šobe in vpliva njene oblike ter interakcije toka plina v realnih pogojih nanašanja. Uporabljen je bil tridimenzionalni CFD-model s sledenjem delcev. Model vključuje tudi substrat na ustrezni razdalji od šobe in tako upošteva nastanek zastojnega tlaka, povratni tok plina in učinke toka v bližini stene. Analizirani sta bili dve obliki šob: ozka šoba (β = 24°) in široka šoba (β = 35°), pri različnih hitrostih nosilnega in oblikovalnega plina ter konstantni hitrosti zaščitnega plina. Konvergenca curka prahu je bila ovrednotena z večplastno metodo štetja delcev in analizirana na podlagi porazdelitve njihove številske gostote v območju gorišča. Rezultati kažejo, da oblika šobe pomembno vpliva na konvergenco curka prahu. Ozka šoba je dosledno zagotavljala kompakten in osno simetričen curek prahu z večjim izkoristkom prahu, medtem ko je široka šoba povzročila bolj razpršen curek prahu in slabšo konvergenco. Ugotovljeno je bilo tudi, da previsoke hitrosti oblikovalnega plina poslabšajo konvergenco zaradi širjenja območja zastojnega tlaka nad substratom. Ugotovitve raziskave predstavljajo fizikalno utemeljeno osnovo za izbiro oblike zvezne koaksialne šobe za DED proces.*

Ključne besede *usmerjeno nanašanje (DED), dodajalna izdelava, sledenje delcev, zasnova zvezne koaksialne šobe*